Chemical Science

ROYAL SOCIETY OF CHEMISTRY

EDGE ARTICLE

View Article Online
View Journal | View Issue

Cite this: *Chem. Sci.*, 2025, **16**, 5155

All publication charges for this article have been paid for by the Royal Society of Chemistry

Logic-gated approach for targeted delivery and site-selective activation of photothermal agents in precision cancer treatment†

Chang Jiang, Zhengxiang Zhao, Amanda K. East, Suritra Bandyopadhyay, Ziyi Jiang and Jefferson Chan *

Received 5th December 2024
Accepted 2nd February 2025

DOI: 10.1039/d4sc08228a

rsc.li/chemical-science

Logic-gated strategies represent a promising approach to achieving highly selective cancer therapies. In this work, we present LG-AB (Logic-Gated Aza-BODIPY), an OFF–ON photothermal therapy (PTT) agent designed to selectively target cancer cells. LG-AB undergoes a red-shift in its maximum absorbance wavelength when activated in the tumor microenvironment, enabling the molecule to precisely generate heat in the cancerous tissue upon light irradiation. Unlike conventional activatable agents that rely on a single biomarker, LG-AB employs an AND logic-gated design, where glucose transporter 1 (GLUT1) overexpression facilitates targeted cellular uptake in cancer cells, followed by activation through elevated glutathione (GSH) levels. Beyond demonstrating photothermal efficacy in human lung cancer and murine breast cancer cells, we show that LG-AB effectively attenuates cancer progression through heat-induced apoptosis, with minimal off-target effects to surrounding tissues. The versatility of this strategy is further demonstrated through the development and application of LG-CPT (Logic-Gated Camptothecin), which utilizes the same logic-gated design. Our results show that enhancing specificity and limiting collateral damage can be broadly applied across different therapeutic agents.

Introduction

Cancer remains one of the leading causes of death worldwide.[1,2] Despite the development of new anticancer therapies, many treatments still suffer from off-target effects, leading to unforeseen safety concerns.[3–6] For instance, in 2022, the FDA withdrew Ukoniq (umbralisib) and several other anticancer drugs after clinical trials revealed an increased risk of death during use.[7] These incidents underscore the urgent need to explore alternative modalities that may offer more precise cancer targeting.

Photothermal therapy (PTT) offers a promising method for targeting cancer cells by using focused light to irradiate a PTT agent, leading to cell death *via* a local temperature increase.[8–12] Although cells have evolved mechanisms such as the expression of heat shock proteins to safeguard against the effects of excessive heating,[13] the rapid temperature rise associated with PTT can overwhelm these protective systems. Specifically, as the temperature increases, cells sequentially experience mild hyperthermia (40–43 °C) which induces cellular stress and enhances permeability; moderate hyperthermia (43–50 °C) which leads to protein denaturation and triggers apoptosis; and severe hyperthermia (50–60 °C) which causes necrosis and rapid cell death.[14–16]

While theoretically PTT offers enhanced cancer selectivity, adjacent tissue can still be harmed due to off-target uptake of PTT agents during treatment. For example, gold nanorods which are commonly used in PTT, can pool in the liver and spleen,[17–20] leading to potential toxicity. To address this challenge, two approaches have been explored. The first strategy involves equipping PTT agents with ligands that target cell surface receptors.[21–27] The second approach employs triggers that respond to and become activated by a given cancer property (*i.e.*, elevated ROS).[28–32] Upon activation, the agent's heat generation capability is enhanced leading to an OFF–ON PTT effect. Unfortunately, the cancer biomarkers in both instances are not exclusive to cancer cells.

In this work, we introduce a novel AND logic gate strategy that requires sequential conditions to be met before PTT is switched on (Scheme 1). The first condition leverages the fact that cancer cells overexpress glucose transporter 1 (GLUT1) owing to their heightened glucose metabolism.[33–39] The second condition is the presence of glutathione (GSH) in its reduced form which is also elevated in cancer cells due to their role in the oxidative stress response.[40–42] Since both GLUT1 and GSH levels are generally lower in healthy cells[36,42] respectively, the likelihood of a PTT agent reaching a healthy cell and becoming activated decreases substantially. To assess the potential of this

Department of Chemistry, Beckman Institute for Advanced Science and Technology, Cancer Center at Illinois, University of Illinois at Urbana-Champaign, Urbana, Illinois 61801, USA. E-mail: jeffchan@illinois.edu

† Electronic supplementary information (ESI) available: Detailed procedures, characterization, and NMR spectra. See DOI: https://doi.org/10.1039/d4sc08228a

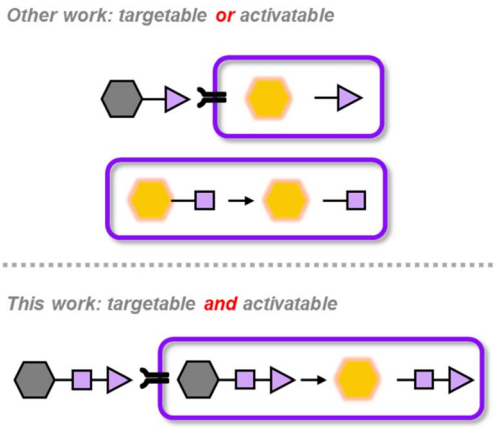

Scheme 1 Comparison table.

logic-gated strategy for achieving greater precision and safety, we developed two therapeutic agents: LG-AB (Logic Gate Aza-BODIPY), an activatable PTT agent, and LG-CPT (Logic Gate Camptothecin), a chemotherapeutic prodrug. LG-AB undergoes a shift in its wavelength of maximum absorbance upon activation which enables effective heat-induced apoptosis with minimal damage to surrounding tissues. Similarly, LG-CPT shows enhanced targetability and reduced off-target effects due to its logic-gated activation mechanism. Both drugs were shown to be efficacious in multiple cancer cell lines and their corresponding murine tumor models.

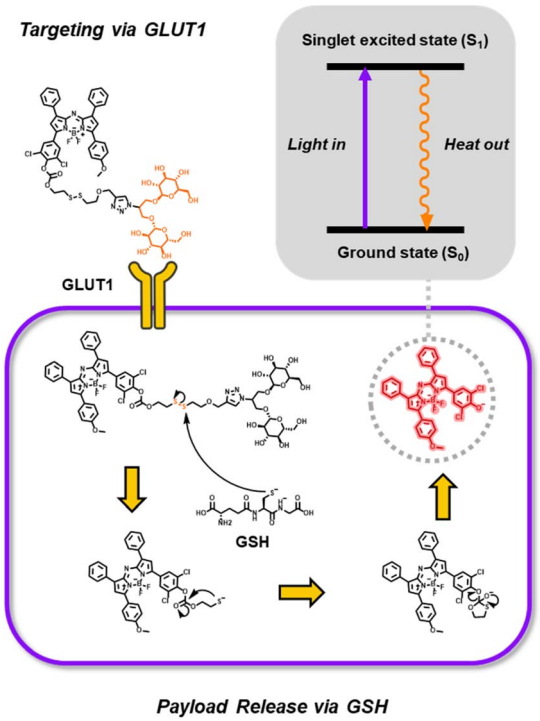

Fig. 1 Schematic illustrating logic-gated design for activatable photothermal therapeutic agent and drug delivery. Payload release relies on sequential targeting of GLUT1 and intracellular glutathione *via* the mvGlu ligand and disulfide trigger, respectively.

Results and discussion

Design and synthesis of LG-AB

LG-AB is composed of two critical design components (Fig. 1). The first component is a light-harvesting unit capable of converting absorbed light into localized heating through a non-radiative decay pathway. For this purpose, we chose the aza-BODIPY dye platform due to its strong absorption in the near-infrared (NIR) region and its large extinction coefficient of 10^4 to 10^5 M^{-1} cm^{-1}.[43–54] These properties are ideal for PTT applications because they enable deeper tissue penetration while minimizing the required concentration of the PTT agent.[10,55] Additionally, by incorporating a 2,6-dichlorophenol moiety ($pK_a \approx 4.35$),[56] we can control the probe's 'off' and 'on' states due to the well-resolved absorbance profiles of the probe and its product. Specifically, capping the aza-BODIPY with any biomarker-responsive trigger capable of blocking in internal charge transfer results in a blue-shifted λ_{abs} and this represents the probes 'off' state. Upon removal of the trigger, the probe will undergo a bathochromic shift and a decrease in fluorescence quantum yield, which enhances heat generation. This design allows precise control over the location of heating by using a laser of wavelength that specifically excites the activated agent AB, rather than the prodrug LG-AB, ensuring targeted thermal treatment of the tissue of interest.

The second component is a trigger designed to effectively cap the aza-BODIPY dye. Traditionally, such triggers respond to a single, carefully selected biomarker.[47,48] However, as mentioned previously, we hypothesize that greater cancer selectivity can be achieved by employing a logic-gated design that first targets GLUT1 on the cell surface and then responds to elevated reduced GSH within the cell. Moreover, our trigger consists of mvGlu, a GLUT1-targeting ligand containing two glucose units connected *via* glycosidic bonds to the primary alcohols of glycerol. Compared to a monosaccharide ligand, the display of two glucose units substantially improves interactions with GLUT1.[44] Additionally, mvGlu is attached to the dye *via* a disulfide linker that can be cleaved by GSH. We hypothesize that due to the proximity and bulkiness of the aza-BODIPY and mvGlu, this disulfide will be more resistant to extracellular GSH attack, which is crucial for limiting off-target release while in circulation ([GSH] $\approx$ 0.1 mM).[57] However, once inside a cancer cell where GSH levels are much higher, GSH will cleave the disulfide and the resulting thiolate will undergo a spontaneous intramolecular cyclization event to release the uncapped aza-BODIPY (Fig. 1).

The synthesis of LG-AB began by treating 2-hydroxyethyl disulfide with sodium hydride and propargyl bromide to afford the mono-propargylated intermediate (**3**). The free alcohol was then activated with phosgene, and the resulting chloroformate formed *in situ*, was reacted with the aza-BODIPY dye prepared separately according to published protocols.[45,56] The capped dye (**4**) was obtained in 90% yield. In parallel, the mvGlu fragment was prepared starting from the acetylation of glucose to yield the peracetylated sugar (**6**) in 90% yield. The anomeric position

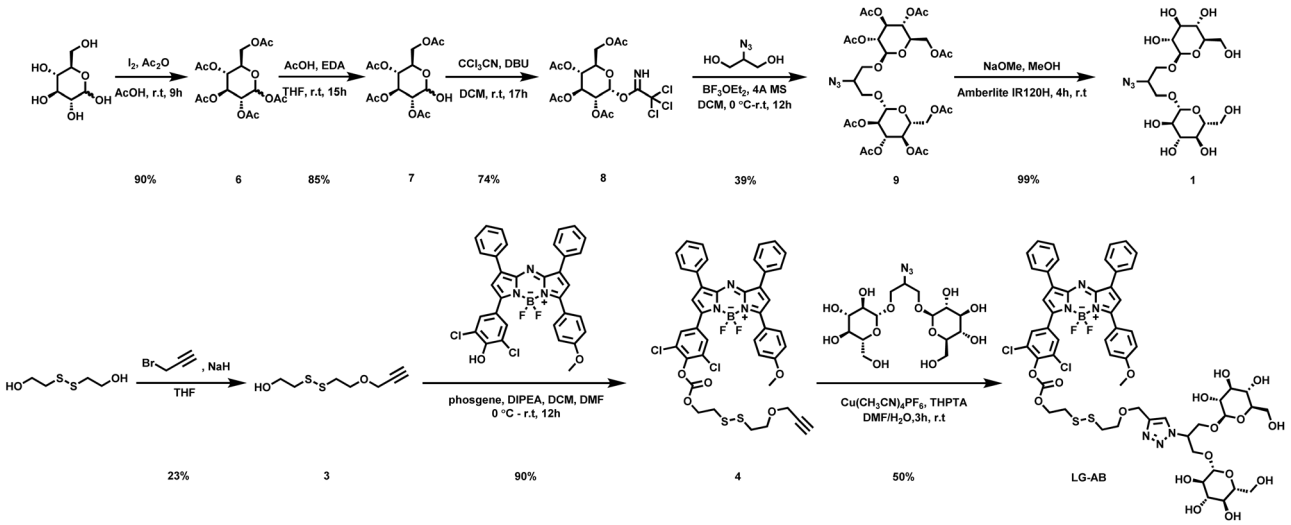

Scheme 2 Synthesis of azido mvGlu and LG-AB.

was selectively deprotected in 85% yield and activated as the trichloroacetimidate (**8**) in 74% yield. 2-Azidoglycerol was then bis-glycosylated using two equivalents of the activated sugar to furnish the protected mvGlu (**9**) in 39% yield. Next, the acetyl groups were globally deprotected using standard Zemplén deacetylation conditions to afford (**1**) in 98.9% yield. Finally, compounds (**1**) and (**4**) were then linked *via* Cu-catalysed azide–alkyne cycloaddition to give LG-AB in 50% yield (Scheme 2).

In vitro photophysical characterization

With LG-AB and its turnover product (AB) in hand, we performed *in vitro* photophysical characterization to assess their ability to absorb light and generate heat. First, we observed that AB exhibits a larger extinction coefficient and a lower fluorescent quantum yield than LG-AB (Table 1). As mentioned above, both properties favor heat generation. Moreover, λ_{max} of AB is at 749 nm, representing a bathochromic shift of 84 nm relative to LG-AB (λ_{abs} = 665 nm). This separation is suitable for enabling selective excitation of AB in the presence of LG-AB. To evaluate this property, samples of LG-AB and AB in PBS (5 μM) were separately inserted into an agar-based tissue-mimicking phantom. Both samples were then irradiated simultaneously at 800 nm using a pulse laser from a multispectral optoacoustic tomography (MSOT) system. The ability of the dyes to absorb this light and release the energy as heat was recorded as ultrasound (*via* the photoacoustic effect). As shown in Fig. 2a, a strong signal was observable from AB, whereas the corresponding readout from LG-AB was only 19 ± 1% of AB.

Table 1 Summary of photophysical properties including λ_{abs}, λ_{em}, ε, and Φ of LG-AB and AB

	λ_{abs}	λ_{em}	ε ($\times 10^4$ M^{-1} cm^{-1})	Φ
LG-AB	665	695	5.02	0.28
AB	749	800	6.82	<0.001

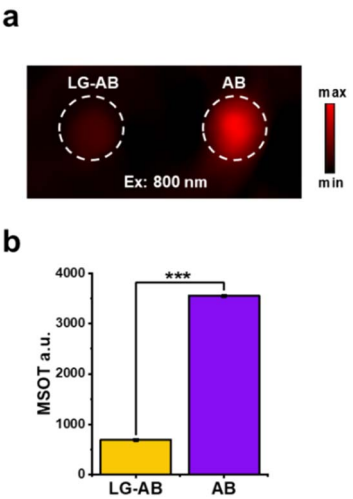

Fig. 2 (a) PA tissue-mimicking phantom images of LG-AB and the turn-over product AB (5 μM) in 1 : 1 v/v MeCN/PBS (pH = 7.4). (b) Quantified data from panel (a). n = 3. Error bars = SD. Statistical analysis was performed using a two-tailed t-test (α = 0.05, $^{**}P < 0.01$, $^{***}P < 0.001$).

Next, we examined the PTT properties of LG-AB and AB using an 808 nm NIR laser. This wavelength was chosen because it is commonly used in PTT for deep tissue penetration with minimal interference from hemoglobin and water. The starting temperature of all samples was 23 °C. After 10 minutes of irradiation, the final temperatures of the samples (80 μM) were as follows: PBS control (28.8 ± 0.4 °C), LG-AB (42.5 ± 0.5 °C), and AB (58.7 ± 0.3 °C) (Fig. 3c). These results indicate that AB generates significantly more heat than LG-AB which reaches the severe hyperthermia range, aligning with our design criteria. Next, we observed a dose- and power-dependent response with AB. Even at reduced concentrations (40 μM and 20 μM) and varying light intensities (1 W cm^{-2}, 2.5 W cm^{-2}, and 4 W cm^{-2}) AB continued to generate a significant amount of heat (Fig. 3d and e). Lastly, we subjected AB to four consecutive irradiation-

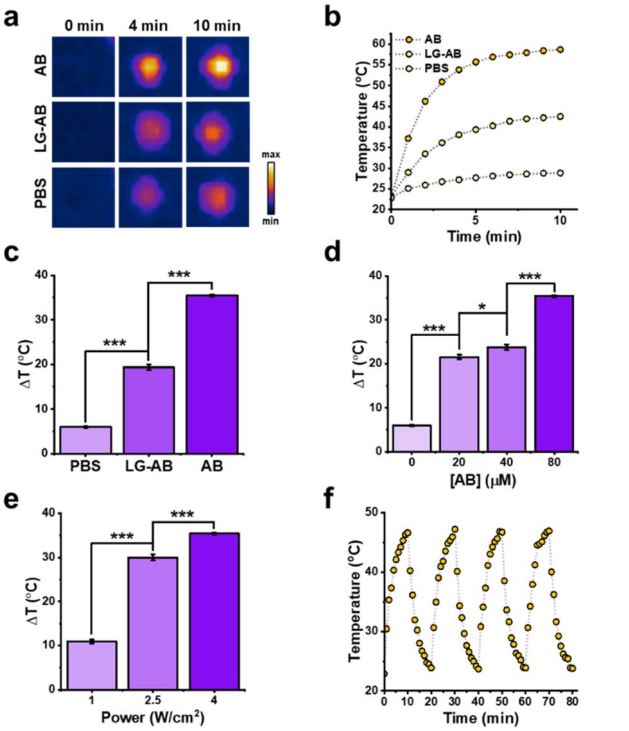

Fig. 3 (a) Thermal images of AB and LG-AB (80 μM) in aqueous solution under 808 nm irradiation (4 W cm^{-2}). (b) Quantified data from panel (a). (c) Quantified data at 10 minutes from panel (a). $n = 3$. Error bars = SD. (d) Temperature variation of different concentrations of AB upon the irradiation of 808 nm. (e) Temperature variation of AB (80 μM) upon different power of irradiation. (f) Temperature evolutions of AB (40 μM) under irradiation (4 W cm^{-2}) during four laser on/off cycles (10 minutes per cycle).

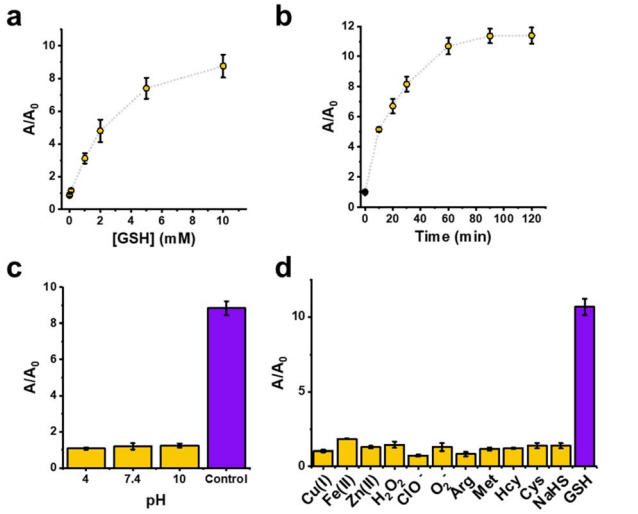

Fig. 4 (a) Time-dependent activation of LG-AB with GSH at 10 mM. (b) Dose-dependent activation of LG-AB with GSH at 0.1–10 mM. (c) pH stability of LG-AB compared to 10 mM GSH positive control. (d) Reactivity of LG-AB with biologically relevant metals, amino acids, reactive oxygen species and thiols after incubation for 1 h at 37 °C. All assays were performed at pH 7.4, 50% PBS/MeCN. Data are presented as mean values ± SD ($n = 3$ independent experiments).

heating cycles, where each cycle involved 10 minutes of irradiation followed by a cooling period. AB maintained consistent temperature increases in each cycle without any noticeable degradation in performance which indicates excellent photo- and thermal-stability (Fig. 3f). Collectively, these experiments demonstrate the feasibility of our aza-BODIPY capping strategy for achieving activatable PTT agents.

Validation of GSH-mediated activation of LG-AB

After confirming that LG-AB possesses the desired photothermal properties, we shifted our focus to assessing its responsiveness to GSH. It is well-established that the reactivity of disulfide bonds can vary significantly based on their chemical structure.[58–61] Given the bulky nature of the peripheral aza-BODIPY and mvGlu moieties, we posit that the disulfide bond in our trigger will be sufficiently stable to resist extensive cleavage by GSH while in circulation. To test this hypothesis, we incubated LG-AB with varying concentrations of GSH (0.1, 1.0, 2.5, 5.0, and 10 mM) for one hour (Fig. 4a). Negligible turnover was observed at 0.1 mM GSH, while at 10 mM GSH activation neared completion within the same timeframe (Fig. 4b). To further evaluate this property, we treated LG-AB with 0.1 mM GSH and monitored the formation of AB for up to 24 hours. Even after extended incubation, less than 45 ± 8% of LG-AB was converted to the product (Fig. S2†).

Considering that LG-AB will encounter various pH environments (acidic and basic) while in circulation, we exposed LG-AB to a range of pH conditions (4 to 10) for 1 hour. Our results show no off-target activation due to pH (Fig. 4c). Finally, beyond GSH and pH, we also examined the stability of LG-AB against a panel of biologically relevant analytes (Fig. 4d). For instance, metal ions such as Cu(I), Fe(II), and Zn(II) can act as Lewis acids, potentially rendering the carbonate linkage more prone to hydrolysis. Similarly, reactive oxygen species including hydrogen peroxide, perchlorate, and superoxide could oxidize the disulfide bond or other components of LG-AB that may lead to premature activation. Finally, other biological thiols such as cysteine, homocysteine, and hydrogen sulfide were also included. When each of these analytes were evaluated at their reported cellular concentrations, no significant activation of LG-AB compared to GSH treatment was observed. Collectively, our results show that LG-AB is predominantly responsive to GSH, with minimal interference from other environmental factors.

Validation of GLUT1-mediated uptake

Encouraged by the promising *in vitro* results, we proceeded to cell studies with the primary objective of assessing the efficacy of GLUT1 targeting. For this purpose, we selected A549 human lung cancer cells, which exhibit elevated GLUT1 expression.[62,63] To begin, we saturated GLUT1 in these cells by incubating them with D-glucose at a concentration of 15 mM for 30 minutes prior to the addition of LG-AB. If the uptake of LG-AB involves GLUT1, we would expect to observe a decrease in the fluorescence signal. Indeed, analysis of our results indicated that vehicle-treated cells

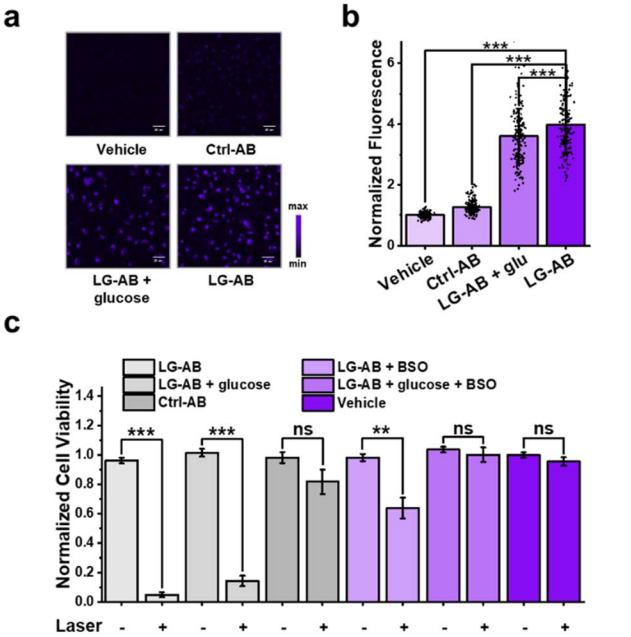

Fig. 5 (a) Representative fluorescent images of A549 human lung cancer cells treated with vehicle (DMSO), LG-AB, LG-AB + glucose, or Ctrl-AB. (b) Quantified data from panel (a). (c) Cytotoxicity assays of 4T1 murine breast cancer cells under different conditions with and without 808 nm irradiation for 10 min. Data are presented as mean values ± SD ($n = 3$ independent experiments).

exhibited ~10% higher fluorescence intensity compared to the glucose-saturated cells (Fig. 5a). We attribute this relatively small effect to the inability to effectively inhibit mvGlu-GLUT1 interactions. Importantly, a larger effect was observed when these experiments were repeated in 4T1 murine breast cancer cells, another cell line with high GLUT1 expression (Fig. S3†). To address this, we developed Ctrl-AB, where the D-glucose moieties were replaced with L-glucose units, which are not recognized by GLUT1. When A549 cells (and 4T1 cells) were stained with LG-AB or Ctrl-AB, a notable difference was observed. Specifically, A549 cells treated with LG-AB were 4-fold brighter than those treated with the control, confirming that the increased fluorescence was indeed GLUT1-mediated.

Next, we conducted cell localization studies to further elucidate GLUT1 involvement. Given the large size of LG-AB direct passage through GLUT1 is unlikely. Instead, we hypothesized that mvGlu interacts with GLUT1, prolonging LG-AB's residency time at the cell membrane, thereby facilitating its internalization *via* phagocytosis. Consistent with this hypothesis, co-staining with commercially available endosomal markers revealed both plasma membrane and endosomal staining patterns (Fig. S5†). Importantly, similar results were observed when these experiments were repeated in 4T1 cells (Fig. S6†).

PTT efficacy in cancer cells

To further demonstrate LG-AB's potential as a PTT agent, we first conducted MTT and trypan blue cell viability studies in both A549 human lung cancer cells and 4T1 murine breast cancer cell lines to establish baseline toxicity. Up to a maximum concentration of 50 μM and 12 hour incubation, no loss of cell viability was observed. Further, a complementary study was performed to show that LG-AB, Ctrl-AB, and the vehicle exhibited no significant toxicity in absence of irradiation (Fig. S7 and S8†).

Next, a new set of cells was incubated with LG-AB, Ctrl-AB, or the vehicle for two hours, followed by washing with PBS. The cells were then irradiated at 808 nm for ten minutes. Trypan blue assays were conducted to determine cell viability. Of note, this protocol was employed due to its ability to provide a rapid and direct assessment of cell membrane integrity, allowing us to quickly and reliably determine the immediate effects of PTT treatment on cell viability. The results showed that LG-AB killed up to 95% of the cells upon irradiation, while cells treated with Ctrl-AB and the vehicle control retained high viability after the same treatment (Fig. 5c). In contrast, when the experiment was repeated in HEK293T cells, LG-AB was found to be 13.4 times less toxic, with 67% cell viability observed in HEK293T cells compared to 5% in 4T1 cells. This difference is attributed to the low levels of GLUT1 expression and intracellular GSH in this non-cancerous cell line (Fig. S13†).

To further validate that the observed PTT efficacy was linked to GLUT1 targeting and GSH-mediated activation, we conducted a series of additional experiments. First, GLUT1 was saturated as before with D-glucose prior to LG-AB treatment and light exposure. Blocking GLUT1 engagement significantly impaired PTT efficacy as evidenced by an increase in cell viability to approximately 14%. Similarly, when we pre-treated cells with buthionine sulfoximine (BSO) to inhibit intracellular GSH biosynthesis prior to PTT treatment, cell viability improved significantly to 64 ± 7% compared to the control. Finally, when cells were co-treated with D-glucose and BSO, we found that PTT efficacy was further reduced, with cell viability improving to nearly 100%. These critical findings confirm that both GLUT1-mediated uptake and GSH activation are essential for the optimal photothermal activity of LG-AB in cancer cells.

In vivo application of LG-AB for PTT

To evaluate the targeting efficacy of LG-AB *in vivo*, we conducted NIR fluorescence imaging studies in a murine model of cancer to simultaneously visualize the liver and tumor sites in Nu/J mice. Off-target accumulation in the liver is common for many small-molecule agents, and we hypothesized that the presence of mvGlu could shift biodistribution toward favoring tumor uptake and retention. Our imaging data revealed that LG-AB rapidly accumulated in both the liver and tumor sites. However, a notable difference in clearance rates was observed between the two. In particular, the fluorescence signal in the liver began to diminish rapidly within 12 hours, the signal in the tumor persisted for an extended period (up to at least 1 week) as indicated by the tumor-to-liver signal ratios plotted as a function of time (Fig. S9†). Given the photo- and thermal-stability of LG-AB, it may be possible to perform multiple rounds of light exposure per single dose of the PTT agent.

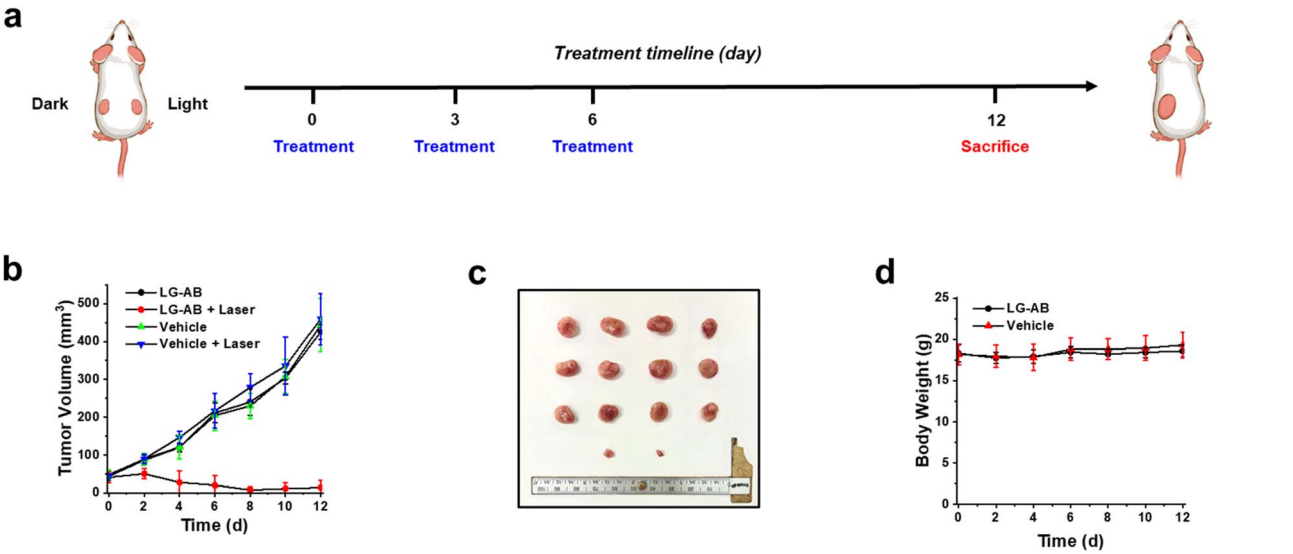

Fig. 6 (a) Timeline of LG-AB PTT treatment on 4T1 tumor-bearing Balb/c mice. (b) Relative tumor volumes in different treatment groups. (c) Tumor images from top to bottom: vehicle, vehicle + laser, LG-AB, LG-AB + laser. (d) Mice's body weight under different conditions. All data are reported as the mean ± SD ($n = 4$ independent experiments).

Next, we inoculated female BALB/c mice (6–8 weeks old) on both flanks with 4T1 cells to generate subcutaneous breast tumors. We opted for a syngeneic model because the innate immune system has been shown to influence the efficacy of PTT treatments.[64] After the tumors had reached a volume of ~50 mm^3, as determined by caliper measurements, LG-AB was administered systemically. After five hours, the tumor on one flank was subjected to light irradiation at 808 nm. The non-irradiated flank served as the dark control. This protocol was repeated on days 3 and 6 for a total of three treatments (Fig. 6a). Another cohort of tumor-bearing mice was treated with a vehicle control and subjected to the same conditions. After the third treatment, all animals were monitored for an additional six days to assess changes in body weight and tumor volume (Fig. 6b–d). No significant change in weight was observed in either group. However, while the tumor volume in the treatment group remained stable, the tumor volume in the dark control group increased to ~400 cm^3. Likewise, the animals receiving the vehicle control also featured tumors in the similar size range. At the end of the study, the tumors were excised, and their weights were recorded to corroborate the measurements taken during the experiment. Additionally, vital organs and surrounding healthy tissue adjacent to the tumors were harvested for H&E staining (Fig. S10†). Our results indicate that cell death occurred only at the tumor site where light was administered, as there was no discernible difference observed in other parts of the body.

Design, evaluation, and *in vivo* application of LG-CPT

To demonstrate the generalizability of the new GLUT1 targeting, GSH-responsive trigger, we modified camptothecin (CPT), a potent topoisomerase I inhibitor,[65] by connecting it to the tertiary alcohol *via* a carbonate linkage to yield LG-CPT. In parallel, we also prepared a control compound, Ctrl-CPT, using L-glucose as described previously. Synthetic protocols, as well as characterization for all intermediates and final compounds can be found in the ESI.† After preparation, both compounds were assessed for cytotoxicity *via* MTT assays in A549 human lung cancer cells and 4T1 murine breast cancer cells. Our results revealed that in 4T1 cells, LG-CPT was approximately 2.41 ± 0.35 times more toxic than Ctrl-CPT. Similarly, in A549 cells, LG-CPT demonstrated 2.61 ± 1.09 times greater toxicity compared to Ctrl-CPT (Table 2). These findings confirm the effectiveness of the GLUT1–GSH targeting strategy in enhancing the selectivity and efficacy of the drug.

Table 2 Summary of IC_{50} and log $D_{7.4}$ of LG-CPT, Ctrl-CPT, and CPT

	IC_{50} (μM) A549	IC_{50} (μM) 4T1	log $D_{7.4}$ octanol/PBS
LG-CPT	0.138 (±0.044)	0.337 (±0.026)	−0.42 ± 0.02
Ctrl-CPT	0.360 (±0.084)	0.813 (±0.065)	—
CPT	0.045 (±0.010)	0.039 (±0.012)	1.75 ± 0.08

Beyond cell viability, we also performed a wound-healing assay to assess the ability of each compound (LG-CPT or Ctrl-CPT) to inhibit cell migration, a crucial process in cancer metastasis. A549 cells were plated onto 48-well plates, and a uniform scratch was created using a p200 pipette tip (Fig. 7a). The extent of wound healing was observed over a 24 hour period. Inhibition of wound healing indicates the compounds' potential to prevent cell migration and proliferation. Our observations revealed that, relative to the vehicle, LG-CPT significantly inhibited wound healing compared to Ctrl-CPT, further supporting its enhanced efficacy in targeting cancer cells through the GLUT1–GSH mechanism (Fig. 7b). Similar observation was found in 4T1 cells as well (Fig. S11†).

Lastly, we generated subcutaneous 4T1 tumors in BALB/c mice. Ten days after inoculation, the first treatment of LG-CPT was administered, followed by two additional doses every

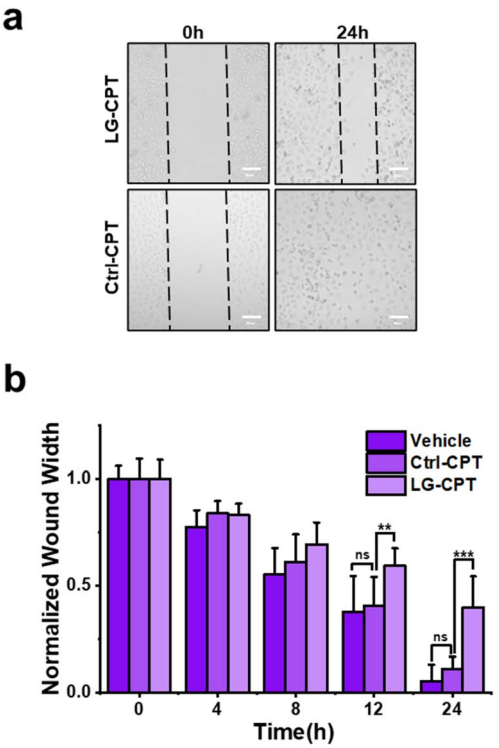

Fig. 7 (a) Representative images of A549 wound-healing assay. (b) Quantified data from panel (a). Data are presented as mean values ± SD (n = 3 independent experiments).

three days. On day 20 post-inoculation, the animals were sacrificed, and their tumors, along with vital organs, were harvested for analysis. Compared to the vehicle-treated group, the tumors in the LG-CPT-treated animals were notably smaller. Interestingly, H&E staining of the heart, intestine, kidney, liver, lung, and spleen revealed no discernible differences between the treated and control groups (Fig. S12†). Moreover, the body weights of the animals in both groups remained consistent throughout the study. These results demonstrate that while LG-CPT significantly inhibited tumor growth, it did not cause any detectable off-target effects or systemic toxicity (Fig. 8).

Conclusions

The development of the GLUT1–GSH logic-gated system represents a significant advancement in the field of targeted cancer therapy. Traditional targeted therapies or prodrug designs often rely on a single biomarker. While this can be effective, the possibility of undesirable side effects owing to off-target delivery and activation remains a concern. Our approach addresses this limitation by incorporating a dual-biomarker strategy,[66–78] thereby enhancing selectivity and reducing the likelihood of unintended targeting and activation in healthy tissues. The logic-gated design of LG-AB and LG-CPT exemplifies the versatility of this approach. For instance, we observed significant cytotoxicity in multiple cancer cell lines; however, when GLUT1 targeting was blocked or GSH-mediated activation was attenuated, drug efficacy was correspondingly reduced. Additionally, we conclusively demonstrated the safety of our approach in non-cancerous mammalian cells. Furthermore, our *in vivo* studies in BALB/c mice bearing 4T1 tumors demonstrated that different modalities could be exploited to effectively inhibit tumor growth without causing detectable off-target effects. However, the current study is limited by species-specific differences in CPT toxicity, as adverse effects on liver function and white blood cell counts commonly observed in humans are not replicated in murine models. Consequently, we were unable to fully demonstrate the advantages of converting CPT to LG-CPT in this context. To address this limitation, future work will focus on incorporating alternative payloads with well-

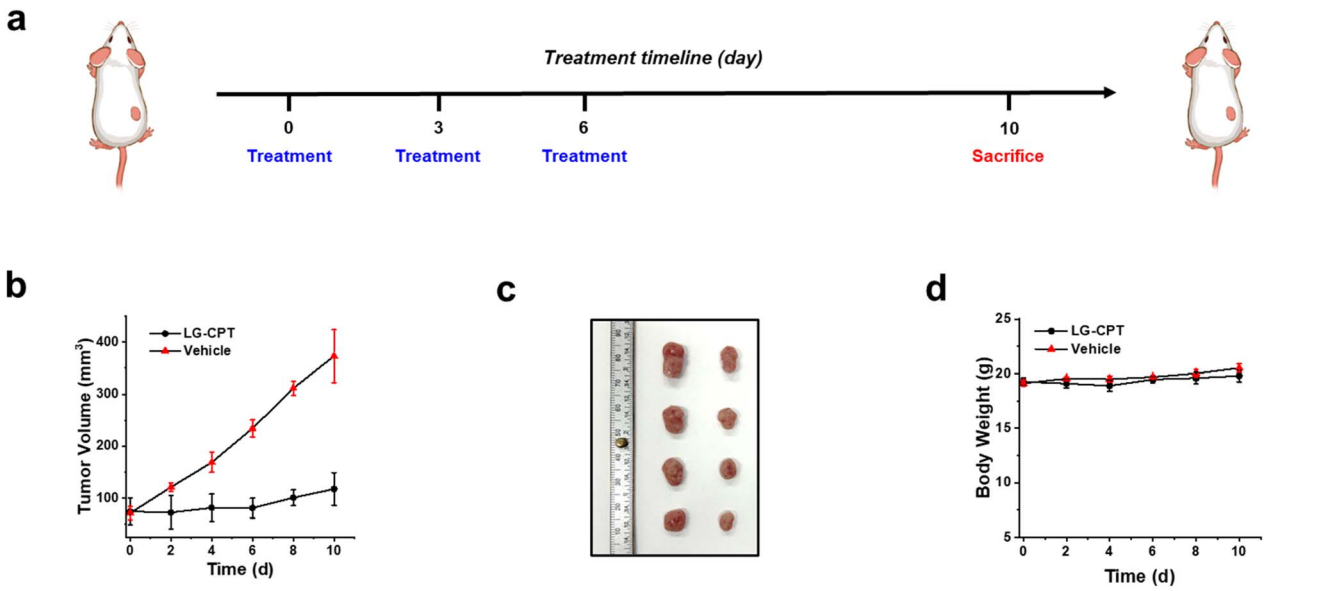

Fig. 8 (a) Timeline of LG-CPT treatment on 4T1 tumor-bearing Balb/c mice. (b) Relative tumor volumes in different treatment groups. (c) Tumor images from left to right: vehicle, LG-CPT. (d) Mice's body weight under different conditions. All data are reported as the mean ± SD (n = 4 independent experiments).

characterized toxicities in mice, providing clearer evidence of how the logic-gated system can effectively minimize systemic toxicity.

That said, the development of this system was not without challenges, as selecting appropriate complementary targets is critical. For instance, if a biomarker is present at exceedingly low levels, the approach may achieve high selectivity but fail to provide sufficient activation for effective cargo delivery. Furthermore, incorporating multiple components to target each biomarker necessitates careful consideration of synthetic accessibility, molecular size, biocompatibility, and formulation stability for *in vivo* use. To overcome these challenges, we strategically identified distinct functional groups: one optimized for targeting and the other for activation, striking a balance between efficacy and practicality. These lessons provide valuable insights for the future development of logic-gated therapeutic platforms.

Beyond PTT agents and potential anticancer drugs, we envision that this strategy can be adapted to a wide range of treatment modalities to yield next-generation cancer therapies. By tailoring the logic gate to different biomarkers, it is possible to design drugs that are highly specific to various cancer types. In conclusion, the integration of a logic-gated trigger in the design of cancer therapeutics offers a promising solution to the challenges of selectivity and safety in cancer treatment. The success of the GLUT1–GSH system in both *in vitro* and *in vivo* models provides a strong foundation for further exploration and development of this approach.

Ethical statement

All animal experiments were performed with the approval of the Institutional Animal Care and Use Committee of the University of Illinois at Urbana-Champaign, following the principles outlined by the American Physiological Society on research animal use. The University of Illinois is accredited by the Association for Assessment and Accreditation of Laboratory Animal Care International (AAALAC). USDA registration number: 33-R-0029 NIH animal assurance number: D16-00075 (A3118-01) (expiration 6/30/25) AAALAC: #00766. Accredited campuswide since 2001.

Data availability

Detailed procedures, characterization, and NMR spectra are provided in the ESI.†

Author contributions

CJ synthesized all compounds and conducted all cellular and *in vivo* experiments. ZZ, AKE, SB, and ZJ assisted CJ with various experiments. CJ and JC designed the experiments and analysed the data. Both CJ and JC contributed to writing the manuscript.

Conflicts of interest

The authors declare no conflict of interest regarding the publication of this article.

Acknowledgements

Z. Z. thanks the Pines Graduate Fellowship for support. A. K. E. and S. B. acknowledge the Beckman Institute Graduate Fellowship for financial support. J. C. thanks the Camille and Henry Dreyfus Foundation for support. Major funding for the 500 MHz Bruker CryoProbe was provided by the Roy J. Carver Charitable Trust (Muscatine, Iowa; Grant No. 15-4521) to the School of Chemical Sciences NMR Lab. The Q-Tof Ultima mass spectrometer was purchased in part with a grant from the National Science Foundation, Division of Biological Infrastructure (DBI-0100085).

Notes and references

1 R. L. Siegel, K. D. Miller, N. S. Wagle and A. Jemal, Cancer Statistics, 2023, *Ca-Cancer J. Clin.*, 2023, **73**, 17–48.
2 B. Purohit, A. Kumar, K. Mahato, S. Roy and P. Chandra, Cancer Cytosensing Approaches in Miniaturized Settings Based on Advanced Nanomaterials and Biosensors, in *Nanotechnology in Modern Animal Biotechnology: Concepts and Applications*, Elsevier, 2019, pp. 133–147.
3 J. Zhai, X. Gu, Y. Liu, Y. Hu, Y. Jiang and Z. Zhang, Chemotherapeutic and Targeted Drugs-Induced Immunogenic Cell Death in Cancer Models and Antitumor Therapy: An Update Review, *Front. Pharmacol*, 2023, 1152934, DOI: **10.3389/fphar.2023.1152934**.
4 L. Vitiello, F. Lixi, G. Coco and G. Giannaccare, Ocular Surface Side Effects of Novel Anticancer Drugs, *Cancers*, 2024, 344, DOI: **10.3390/cancers16020344**.
5 J. K. Roydhouse, B. L. King-Kallimanis, P. Roy, C. Weinstock, D. Krol, S. R. Daniels, D. L. Suzman, J. A. Beaver and P. G. Kluetz, Exploration of Baseline Patient-Reported Side Effect Bother from Cancer Therapy, *Clin. Trials*, 2020, **17**, 332–337.
6 J. Tímár and A. Uhlyarik, On-Target Side Effects of Targeted Therapeutics of Cancer, *Pathol. Oncol. Res.*, 2022, 1610694, DOI: **10.3389/pore.2022.1610694**.
7 A. J. Preziosi and R. Priefer, Oncology's Trial and Error: Analysis of the FDA Withdrawn Accelerated Approvals, *Life Sci.*, 2024, 122615, DOI: **10.1016/j.lfs.2024.122615**.
8 C. Li, Y. Cheng, D. Li, Q. An, W. Zhang, Y. Zhang and Y. Fu, Antitumor Applications of Photothermal Agents and Photothermal Synergistic Therapies, *Int. J. Mol. Sci.*, 2022, 7909, DOI: **10.3390/ijms23147909**.
9 D. Zhi, T. Yang, J. O'Hagan, S. Zhang and R. F. Donnelly, Photothermal Therapy, *J. Controlled Release*, 2020, 52–71.
10 Y. Zhang, S. Zhang, Z. Zhang, L. Ji, J. Zhang, Q. Wang, T. Guo, S. Ni, R. Cai, X. Mu, W. Long and H. Wang, Recent Progress on NIR-II Photothermal Therapy, *Front. Chem.*, 2021, 728066, DOI: **10.3389/fchem.2021.728066**.
11 Y. Wang, H. M. Meng, G. Song, Z. Li and X. B. Zhang, Conjugated-Polymer-Based Nanomaterials for Photothermal Therapy, *ACS Appl. Polym. Mater.*, 2020, 4258–4272.
12 S. Guo, T. Guan, Y. Ke, Y. Lin, R. Tai, J. Ye, Z. Deng, S. Deng and C. Ou, Biologically Logic-Gated Trojan-Horse Strategy

for Personalized Triple-Negative Breast Cancer Precise Therapy by Selective Ferroptosis and STING Pathway Provoking, *Biomaterials*, 2025, **315**, 122905, DOI: 10.1016/j.biomaterials.2024.122905.

13 A. Gouda, S. Tolba, K. Mahrose, S. G. Felemban, A. F. Khafaga, N. E. Khalifa, M. Jaremko, M. Moustafa, M. O. Alshaharni, U. Algopish and M. E. Abd El-Hack, Heat Shock Proteins as a Key Defense Mechanism in Poultry Production under Heat Stress Conditions, *Poult. Sci.*, 2024, 103537, DOI: 10.1016/j.psj.2024.103537.

14 M. Chang, Z. Hou, M. Wang, C. Li and J. Lin, Recent Advances in Hyperthermia Therapy-Based Synergistic Immunotherapy, *Adv. Mater.*, 2021, e2004788, DOI: 10.1002/adma.202004788.

15 Y. Zhang, X. Zhan, J. Xiong, S. Peng, W. Huang, R. Joshi, Y. Cai, Y. Liu, R. Li, K. Yuan, N. Zhou and W. Min, Temperature-Dependent Cell Death Patterns Induced by Functionalized Gold Nanoparticle Photothermal Therapy in Melanoma Cells, *Sci. Rep.*, 2018, **8**, 8720, DOI: 10.1038/s41598-018-26978-1.

16 D. Chang, M. Lim, J. A. C. M. Goos, R. Qiao, Y. Y. Ng, F. M. Mansfeld, M. Jackson, T. P. Davis and M. Kavallaris, Biologically Targeted Magnetic Hyperthermia: Potential and Limitations, *Front. Pharmacol*, 2018, 831, DOI: 10.3389/fphar.2018.00831.

17 M. Bartneck, T. Ritz, H. A. Keul, M. Wambach, J. Bornemann, U. Gbureck, J. Ehling, T. Lammers, F. Heymann, N. Gassler, T. Lüdde, C. Trautwein, J. Groll and F. Tacke, Peptide-Functionalized Gold Nanorods Increase Liver Injury in Hepatitis, *ACS Nano*, 2012, **6**, 8767–8777.

18 H. Cai, Y. Ma, Z. Wu, Y. Ding, P. Zhang, X. He, J. Zhou, Z. Chai and Z. Zhang, Protein Corona Influences Liver Accumulation and Hepatotoxicity of Gold Nanorods, *NanoImpact*, 2016, **3–4**, 40–46.

19 R. Robinson, W. Gerlach and H. Ghandehari, Comparative Effect of Gold Nanorods and Nanocages for Prostate Tumor Hyperthermia, *J. Controlled Release*, 2015, **220**, 245–252.

20 V. Ranjan Srivastava, R. Kumari and P. Chandra, Miniaturized Surface Engineered Technologies for Multiplex Biosensing Devices, *Electroanalysis*, 2023, e202200355, DOI: 10.1002/elan.202200355.

21 J. Kadkhoda, A. Aghanejad, B. Safari, J. Barar, S. H. Rasta and S. Davaran, Aptamer-Conjugated Gold Nanoparticles for Targeted Paclitaxel Delivery and Photothermal Therapy in Breast Cancer, *J. Drug Delivery Sci. Technol.*, 2022, **67**, 102954, DOI: 10.1016/j.jddst.2021.102954.

22 H. Wang, J. Chang, M. Shi, W. Pan, N. Li and B. Tang, A Dual-Targeted Organic Photothermal Agent for Enhanced Photothermal Therapy, *Angew. Chem.*, 2019, **131**, 1069–1073.

23 G. Jo, Y. Park, M. H. Park and H. Hyun, Near-Infrared Fluorescent Hydroxyapatite Nanoparticles for Targeted Photothermal Cancer Therapy, *Pharmaceutics*, 2023, **15**, 1374, DOI: 10.3390/pharmaceutics15051374.

24 Y. Zou, M. Li, T. Xiong, X. Zhao, J. Du, J. Fan and X. Peng, A Single Molecule Drug Targeting Photosensitizer for Enhanced Breast Cancer Photothermal Therapy, *Small*, 2020, **16**, e1907677, DOI: 10.1002/smll.201907677.

25 C. Cui, J. Li, J. Fang, Y. Zhao, Y. Zhang, S. Ye, A. Wang, Y. Feng, Q. Mao, H. Qin and H. Shi, Building Multipurpose Nano-Toolkit by Rationally Decorating NIR-II Fluorophore to Meet the Needs of Tumor Diagnosis and Treatment, *Chin. Chem. Lett.*, 2022, **33**, 3478–3483.

26 M. Zhao, J. Ding, Q. Mao, Y. Zhang, Y. Gao, S. Ye, H. Qin and H. Shi, A Novel αvβ3 Integrin-Targeted NIR-II Nanoprobe for Multimodal Imaging-Guided Photothermal Therapy of Tumors: In Vivo, *Nanoscale*, 2020, **12**, 6953–6958.

27 P. Chen, X. Wang, C. Zhu, T. Guo, C. Wang and L. Ying, Targeted Delivery of Quinoxaline-Based Semiconducting Polymers for Tumor Photothermal Therapy, *ACS Appl. Mater. Interfaces*, 2024, **16**, 38377–38386.

28 X. Zhao, S. Long, M. Li, J. Cao, Y. Li, L. Guo, W. Sun, J. Du, J. Fan and X. Peng, Oxygen-Dependent Regulation of Excited-State Deactivation Process of Rational Photosensitizer for Smart Phototherapy, *J. Am. Chem. Soc.*, 2020, **142**, 1510–1517.

29 X. Gao, S. Jiang, C. Li, Y. Chen, Y. Zhang, P. Huang and J. Lin, Highly Photostable Croconium Dye-Anchored Cell Membrane Vesicle for Tumor PH-Responsive Duplex Imaging-Guided Photothermal Therapy, *Biomaterials*, 2021, **267**, 120454, DOI: 10.1016/j.biomaterials.2020.120454.

30 T. H. Wang, M. Y. Shen, N. T. Yeh, Y. H. Chen, T. C. Hsu, H. Y. Chin, Y. T. Wu, B. S. Tzang and W. H. Chiang, Photothermal Nanozymes to Self-Augment Combination Cancer Therapy by Dual-Glutathione Depletion and Hyperthermia/Acidity-Activated Hydroxyl Radical Generation, *J. Colloid Interface Sci.*, 2023, **650**, 1698–1714.

31 W. X. Wang, J. J. Chao, Z. Q. Wang, T. Liu, G. J. Mao, B. Yang and C. Y. Li, Dual Key-Activated Nir-I/II Fluorescence Probe for Monitoring Photodynamic and Photothermal Synergistic Therapy Efficacy, *Adv. Healthcare Mater.*, 2023, **12**, e2301230, DOI: 10.1002/adhm.202301230.

32 H. Li, Y. Zhao, Y. Jia, G. Chen, J. Peng and J. Li, PH-Responsive Dopamine-Based Nanoparticles Assembled: Via Schiff Base Bonds for Synergistic Anticancer Therapy, *Chem. Commun.*, 2020, **56**, 13347–13350.

33 Y. Kobayashi, K. Banno, H. Kunitomi, T. Takahashi, T. Takeda, K. Nakamura, K. Tsuji, E. Tominaga and D. Aoki, Warburg Effect in Gynecologic Cancers, *J. Obstet. Gynaecol. Res.*, 2019, **45**, 542–548.

34 P. B. Ancey, C. Contat and E. Meylan, Glucose Transporters in Cancer – from Tumor Cells to the Tumor Microenvironment, *FEBS J.*, 2018, 2926–2943.

35 M. Mueckler and B. Thorens, The SLC2 (GLUT) Family of Membrane Transporters, *Mol. Aspects Med.*, 2013, 121–138.

36 A. Bukkuri, R. A. Gatenby and J. S. Brown, GLUT1 Production in Cancer Cells: A Tragedy of the Commons, *npj Syst. Biol. Appl.*, 2022, **8**, 22, DOI: 10.1038/s41540-022-00229-6.

37 F. R. R. Ayala, R. M. Rocha, K. C. Carvalho, A. L. Carvalho, I. W. Da Cunha, S. V. Lourenço and F. A. Soares, Glut1 and Glut3 as Potential Prognostic Markers for Oral Squamous Cell Carcinoma, *Molecules*, 2010, **15**, 2374–2387.

38 J. Wang, C. Ye, C. Chen, H. Xiong, B. Xie, J. Zhou, Y. Chen, S. Zheng and L. Wang, Glucose Transporter GLUT1 Expression and Clinical Outcome in Solid Tumors: A Systematic Review and Meta-Analysis, *Oncotarget*, 2017, **8**, 16875–16886.

39 P. R. Vernekar, B. Purohit, N. P. Shetti and P. Chandra, Glucose Modified Carbon Paste Sensor in the Presence of Cationic Surfactant for Mefenamic Acid Detection in Urine and Pharmaceutical Samples, *Microchem. J.*, 2021, **160**, 105599, DOI: **10.1016/j.microc.2020.105599**.

40 G. Elda Valenti, B. Tasso, N. Traverso, C. Domenicotti and B. Marengo, Glutathione in Cancer Progression and Chemoresistance: An Update, *Redox Experimental Medicine*, 2023, **2023**, e220023, DOI: **10.1530/rem-22-0023**.

41 N. Traverso, R. Ricciarelli, M. Nitti, B. Marengo, A. L. Furfaro, M. A. Pronzato, U. M. Marinari and C. Domenicotti, Role of Glutathione in Cancer Progression and Chemoresistance, *Oxid. Med. Cell. Longevity*, 2013, 972913, DOI: **10.1155/2013/972913**.

42 M. P. Gamcsik, M. S. Kasibhatla, S. D. Teeter and O. M. Colvin, Glutathione Levels in Human Tumors, *Biomarkers*, 2012, 671–691.

43 C. J. Reinhardt, R. Xu and J. Chan, Nitric Oxide Imaging in Cancer Enabled by Steric Relaxation of a Photoacoustic Probe Platform, *Chem. Sci.*, 2020, **11**, 1587–1592.

44 A. K. East, M. C. Lee, C. Jiang, Q. Sikander and J. Chan, Biomimetic Approach to Promote Cellular Uptake and Enhance Photoacoustic Properties of Tumor-Seeking Dyes, *J. Am. Chem. Soc.*, 2023, **145**, 7313–7322.

45 M. Y. Lucero, Y. Tang, C. J. Zhang, S. Su, J. A. Forzano, V. Garcia, X. Huang, D. Moreno and J. Chan, Activity-Based Photoacoustic Probe for Biopsy-Free Assessment of Copper in Murine Models of Wilson's Disease and Liver Metastasis, *Proc. Natl. Acad. Sci. U. S. A.*, 2021, **118**, e2106943118, DOI: **10.1073/pnas.2106943118/-/DCSupplemental**.

46 E. Y. Zhou, H. J. Knox, C. Liu, W. Zhao and J. Chan, A Conformationally Restricted Aza-BODIPY Platform for Stimulus-Responsive Probes with Enhanced Photoacoustic Properties, *J. Am. Chem. Soc.*, 2019, **141**, 17601–17609.

47 Z. Zhao, M. Lucero, S. Su, E. J. Chaney, J. J. Xu, M. Myszka and J. Chan, Activity-based sensing reveals elevated labile copper promotes liver aging via hepatic ALDH1A1 depletion, *Nat. Commun.*, 2025, DOI: **10.1038/s41467-025-56585-4**.

48 A. K. East, M. C. Lee, C. Jiang, Q. Sikander and J. Chan, Biomimetic Approach to Promote Cellular Uptake and Enhance Photoacoustic Properties of Tumor-Seeking Dyes, *J. Am. Chem. Soc.*, 2023, **145**, 7313–7322.

49 E. Y. Zhou, H. J. Knox, C. J. Reinhardt, G. Partipilo, M. J. Nilges and J. Chan, Near-Infrared Photoactivatable Nitric Oxide Donors with Integrated Photoacoustic Monitoring, *J. Am. Chem. Soc.*, 2018, **140**, 11686–11697.

50 H. J. Knox, J. Hedhli, T. W. Kim, K. Khalili, L. W. Dobrucki and J. Chan, A Bioreducible N-Oxide-Based Probe for Photoacoustic Imaging of Hypoxia, *Nat. Commun.*, 2017, **8**, 1794, DOI: **10.1038/s41467-017-01951-0**.

51 E. Y. Zhou, H. J. Knox, C. Liu, W. Zhao and J. Chan, A Conformationally Restricted Aza-BODIPY Platform for Stimulus-Responsive Probes with Enhanced Photoacoustic Properties, *J. Am. Chem. Soc.*, 2019, **141**, 17601–17609.

52 C. J. Reinhardt, E. Y. Zhou, M. D. Jorgensen, G. Partipilo and J. Chan, A Ratiometric Acoustogenic Probe for in Vivo Imaging of Endogenous Nitric Oxide, *J. Am. Chem. Soc.*, 2018, **140**, 1011–1018.

53 H. Li, P. Zhang, L. P. Smaga, R. A. Hoffman and J. Chan, Photoacoustic Probes for Ratiometric Imaging of Copper(II), *J. Am. Chem. Soc.*, 2015, **137**, 15628–15631.

54 H. J. Knox, T. W. Kim, Z. Zhu and J. Chan, Photophysical Tuning of N-Oxide-Based Probes Enables Ratiometric Photoacoustic Imaging of Tumor Hypoxia, *ACS Chem. Biol.*, 2018, **13**, 1838–1843.

55 X. Zhang, S. Li, H. Ma, H. Wang, R. Zhang and X. D. Zhang, Activatable NIR-II Organic Fluorescent Probes for Bioimaging, *Theranostics*, 2022, 3345–3371.

56 H. Li, P. Zhang, L. P. Smaga, R. A. Hoffman and J. Chan, Photoacoustic Probes for Ratiometric Imaging of Copper(II), *J. Am. Chem. Soc.*, 2015, **137**, 15628–15631.

57 F. Q. Schafer and G. R. Buettner, Redox Environment of the Cell as Viewed Through the Redox State of the Glutathione Disulfide/Glutathione Couple, *Free Radical Biol. Med.*, 2001, **30**, 1191–1221.

58 X. Tan, H. Zhou, C. Wang, X. Liu, X. Yang and W. Liu, GSH-Responsive Camptothecin Prodrug-Based Hybrid Micellar Nanoparticles Enable Antitumor Chemo-Immunotherapy by PD-L1 Knockdown, *Nano Res.*, 2023, **16**, 834–848.

59 X. Liu, W. Shao, Y. Zheng, C. Yao, L. Peng, D. Zhang, X. Y. Hu and L. Wang, GSH-Responsive Supramolecular Nanoparticles Constructed by β-d-Galactose-Modified Pillar[5]Arene and Camptothecin Prodrug for Targeted Anticancer Drug Delivery, *Chem. Commun.*, 2017, **53**, 8596–8599.

60 S. Dong, J. He, Y. Sun, D. Li, L. Li, M. Zhang and P. Ni, Efficient Click Synthesis of a Protonized and Reduction-Sensitive Amphiphilic Small-Molecule Prodrug Containing Camptothecin and Gemcitabine for a Drug Self-Delivery System, *Mol. Pharm.*, 2019, **16**, 3770–3779.

61 S. Bhuniya, M. Hee Lee, H. Mi Jeon, J. Hye Han, J. Hong Lee, N. Park, S. Maiti, C. Kang and J. Seung Kim, A Fluorescence Off-on Reporter for Real Time Monitoring of Gemcitabine Delivery to the Cancer Cells, *Chem. Commun.*, 2013, **49**, 7141–7143.

62 C. D. Young, A. S. Lewis, M. C. Rudolph, M. D. Ruehle, M. R. Jackman, U. J. Yun, O. Ilkun, R. Pereira, E. D. Abel and S. M. Anderson, Modulation of Glucose Transporter 1 (GLUT1) Expression Levels Alters Mouse Mammary Tumor Cell Growth in Vitro and in Vivo, *PLoS One*, 2011, **6**, e23205, DOI: **10.1371/journal.pone.0023205**.

63 M. L. Macheda, S. Rogers and J. D. Best, Molecular and Cellular Regulation of Glucose Transporter (GLUT) Proteins in Cancer, *J. Cell. Physiol.*, 2005, **202**, 654–662.

64 M. Wang, M. Chang, P. Zheng, Q. Sun, G. Wang, J. Lin and C. Li, A Noble AuPtAg-GOx Nanozyme for Synergistic Tumor Immunotherapy Induced by Starvation Therapy-

Augmented Mild Photothermal Therapy, *Advanced Science*, 2022, **9**, e2202332, DOI: **10.1002/advs.202202332**.

65 A. Lichota and K. Gwozdzinski, Anticancer Activity of Natural Compounds from Plant and Marine Environment, *Int. J. Mol. Sci.*, 2018, 3533, DOI: **10.3390/ijms19113533**.

66 X. Wang, S. S. Liew, J. Huang, Y. Hu, X. Wei and K. Pu, Dual-Locked Enzyme-Activatable Bioorthogonal Fluorescence Turn-On Imaging of Senescent Cancer Cells, *J. Am. Chem. Soc.*, 2024, **146**, 22689–22698.

67 S. Yang, Y. Wu, W. Zhong, R. Chen, M. Wang and M. Chen, GSH/PH Dual Activatable Cross-Linked and Fluorinated PEI for Cancer Gene Therapy Through Endogenous Iron De-Hijacking and in Situ ROS Amplification, *Adv. Mater.*, 2024, **36**, e2304098, DOI: **10.1002/adma.202304098**.

68 X. Wang, S. He, P. Cheng and K. Pu, A Dual-Locked Tandem Fluorescent Probe for Imaging of Pyroptosis in Cancer Chemo-Immunotherapy, *Adv. Mater.*, 2023, **35**, e2206510, DOI: **10.1002/adma.202206510**.

69 Y. C. Li, D. R. Hu, M. Pan, Y. Qu, B. Y. Chu, J. F. Liao, X. H. Zhou, Q. Y. Liu, S. Cheng, Y. Chen, Q. Wei and Z. Y. Qian, Near-Infrared Light and Redox Dual-Activatable Nanosystems for Synergistically Cascaded Cancer Phototherapy with Reduced Skin Photosensitization, *Biomaterials*, 2022, **288**, 121700, DOI: **10.1016/j.biomaterials.2022.121700**.

70 Y. Hu, J. Yu, M. Xu and K. Pu, Bienzyme-Locked Activatable Fluorescent Probes for Specific Imaging of Tumor-Associated Mast Cells, *J. Am. Chem. Soc.*, 2024, 12656–12663, DOI: **10.1021/jacs.4c02070**.

71 W. Zeng, H. Zhang, Y. Deng, A. Jiang, X. Bao, M. Guo, Z. Li, M. Wu, X. Ji, X. Zeng and L. Mei, Dual-Response Oxygen-Generating MnO2 Nanoparticles with Polydopamine Modification for Combined Photothermal-Photodynamic Therapy, *Chem. Eng. J.*, 2020, **389**, 124494, DOI: **10.1016/j.cej.2020.124494**.

72 J. Huang, M. Xu, P. Cheng, J. Yu, J. Wu and K. Pu, A Tandem-Locked Chemiluminescent Probe for Imaging of Tumor-Associated Macrophage Polarization, *Angew. Chem., Int. Ed.*, 2024, **63**, e202319780, DOI: **10.1002/anie.202319780**.

73 P. Cheng, S. He, C. Zhang, J. Liu and K. Pu, A Tandem-Locked Fluorescent NETosis Reporter for the Prognosis Assessment of Cancer Immunotherapy, *Angew. Chem., Int. Ed.*, 2023, **62**, e202301625, DOI: **10.1002/anie.202301625**.

74 J. Shen, M. Ma, M. Shafiq, H. Yu, Z. Lan and H. Chen, Microfluidics-Assisted Engineering of PH/Enzyme Dual-Activatable ZIF@Polymer Nanosystem for Co-Delivery of Proteins and Chemotherapeutics with Enhanced Deep-Tumor Penetration, *Angew. Chem., Int. Ed.*, 2022, **61**, e202113703, DOI: **10.1002/anie.202113703**.

75 X. Wei, C. Zhang, S. He, J. Huang, J. Huang, S. S. Liew, Z. Zeng and K. Pu, A Dual-Locked Activatable Phototheranostic Probe for Biomarker-Regulated Photodynamic and Photothermal Cancer Therapy, *Angew. Chem., Int. Ed.*, 2022, **61**, e202202966, DOI: **10.1002/anie.202202966**.

76 X. Zhang, Y. Chen, H. He, S. Wang, Z. Lei and F. Zhang, ROS/RNS and Base Dual Activatable Merocyanine-Based NIR-II Fluorescent Molecular Probe for in Vivo Biosensing, *Angew. Chem., Int. Ed.*, 2021, **60**, 26337–26341.

77 A. Baranwal, A. K. Chiranjivi, A. Kumar, V. K. Dubey and P. Chandra, Design of Commercially Comparable Nanotherapeutic Agent against Human Disease-Causing Parasite, Leishmania, *Sci. Rep.*, 2018, **8**, 8814, DOI: **10.1038/s41598-018-27170-1**.

78 U. P. Azad and P. Chandra, *Handbook of Nanobioelectrochemistry: Application in Devices and Biomolecular Sensing*, Springer, 2023, DOI: **10.1007/978-981-19-9437-1**.